

1
2
3
4
5
6
7
8
9
10
11
12
13
14
15
16
17
18
19
20
21
22
23
24
25
26
27
28
29
30
31
32
33
34
35
36
37
38
39
40
41
42
43

**Diapycnal mixing across the photic zone of the
NE-Atlantic**

**by Hans van Haren*, Corina P.D. Brussaard, Loes J. A.
Gerringa, Mathijs H. van Manen, Rob Middag, Ruud
Groenewegen**

Royal Netherlands Institute for Sea Research (NIOZ), P.O. Box 59, 1790 AB Den Burg,
the Netherlands.
*e-mail: hans.van.haren@nioz.nl

Abstract. Variable physical conditions such as vertical turbulent exchange, internal wave and mesoscale eddy action, affect the availability of light and nutrients for phytoplankton (unicellular algae) growth. It is hypothesized that changes in ocean temperature may affect ocean vertical density stratification, which may hamper vertical exchange. In order to quantify variations in physical conditions in the Northeast Atlantic Ocean, we sampled a latitudinal transect along $17\pm5^\circ\text{W}$ between 30 and 62°N in summer. A shipborne Conductivity-Temperature-Depth CTD-instrumented package was used with a custom-made modification of the pump-inlet to minimize detrimental effects of ship motions on its data. Thorpe-scale analysis was used to establish turbulence values for the upper 500 m near the surface from 3 to 6 profiles obtained in a short CTD-yoyo, 3 to 5 h after local sunrise. From south to north, temperature decreased together with stratification while turbulence values weakly increased or remained constant. Vertical turbulent nutrient fluxes across the stratification were not found to significantly vary with latitude. This apparent lack of correspondence between turbulent mixing and temperature is suggested to be due to internal waves breaking and acting as a potential feed-back mechanism. Our findings suggest that nutrient availability for phytoplankton in the euphotic surface waters may not be affected by the physical process of global warming.

1 Introduction

The physical environment is important for ocean life, including variations therein. For example, the sun stores heat in the ocean with a stable vertical density stratification as result. Generally, stratification hampers vertical turbulent exchange because of the required work against (reduced) gravity before turbulence can take effect. It thus hampers a supply of nutrients via a turbulent flux from deeper waters to the photic zone. However, stratification supports internal waves, which (i) may move near-floating particles like phytoplankton (unicellular algae) up- and down towards and away from the surface, and (ii) may induce enhanced turbulence via vertical current differences (shear) resulting in internal waves breaking (Denman and Gargett, 1983). Such changes in the physical environment are expected to affect the availability of phytoplankton growth factors such as light and nutrients.

Climate models predict that global warming will reduce vertical mixing in the oceans (e.g., Sarmiento et al., 2004). Mathematical models on system stability suggest that reduced mixing may generate chaotic behaviour in phytoplankton production, thereby enhancing variability in carbon export into the ocean interior (Huisman et al., 2006). However, none of these models include potential feed-back systems like internal wave action or mesoscale eddy activity. From observations in the relatively shallow North Sea it is known that the strong seasonal temperature stratification is marginally stable, as it supports internal waves and shear to such extent that sufficient nutrients are replenished from below to sustain the late-summer bloom (van Haren et al., 1999). This challenges the current paradigm in climate models.

In this paper, the objective is to resolve the effect of vertical stratification and turbulent mixing on nutrient supply to the photic zone of the open ocean. For this purpose, upper-500-m-ocean shipborne Conductivity-Temperature-Depth CTD-observations were made in association with those on dissolved inorganic nutrients during a survey along a transect in the NE-Atlantic Ocean from mid- to high-latitudes in summer. Throughout the survey, meteorological and sea-state conditions were favourable for adequate sampling and wind speeds varied little between 5 and 10 m s⁻¹, independent of locations. All CTD-observations

were made far from lateral, continental boundaries and at least 1000 m vertically away from bottom topography. The NE-Atlantic is characterized by abundant (sub-)mesoscale eddies especially in the upper ocean (Charria et al., 2017) that influence local plankton communities (Hernández- Hernández et al., 2020). The area also shows continuous abundant internal wave activity away from topographic sources and sinks, with the semidiurnal tide as a main source from below and atmospherically induced inertial motions from above (e.g., van Haren, 2005; 2007). The present research complements research based on photic zone (upper 100 m) observations obtained along the same transect using a slowly descending turbulence microstructure profiler next to CTD-sampling eight years earlier (Jurado et al., 2012). Their data demonstrated a negligibly weak increase in turbulence values with significant decreases in stratification going north. However, no nutrient data were presented and no turbulent nutrient fluxes could be computed. In another study (Mojica et al., 2016), macro-nutrients and their vertical gradients were presented for the upper 200 m and both were found to increase from south to north. The present observations go deeper to 500 m, also across the non-seasonal more permanent stratification. Moreover, coinciding measurements were made of the distributions of macro-nutrients and dissolved iron. This allows vertical turbulent nutrient fluxes to be computed. It leads to a hypothesis concerning a physical feed-back mechanism that may control changes in stratification.

2 Materials and Methods

Between 22 July and 16 August 2017, observations were made from the R/V Pelagia in the Northeast Atlantic Ocean at stations along a transect from Iceland, starting around 60°N, to the Canary Islands, ending around 30°N, (Fig. 1). The transect was more or less in meridional direction, with stations along $17\pm5^\circ\text{W}$, all in the same time zone (UTC-1 h = local time LT). Full water-depth Rosette bottle water sampling was performed at most stations.

Samples for dissolved inorganic macro-nutrients were filtered through 0.2 μm Acrodisc filter and stored frozen in a HDPE pony-vial (nitrate, nitrite and phosphate) or at 4°C (silicate)

116 until analysis. Nutrients were analysed under temperature controlled conditions using a
117 QuAAtro Gas Segmented Continuous Flow Analyser. All measurements were calibrated with
118 standards diluted in low nutrient seawater in the salinity range of the stations to ensure that
119 analysis remained within the same ionic strength. Phosphate (PO_4), nitrate plus nitrite (NO_x),
120 were measured according to Murphy and Riley (1962) and Grasshoff et al. (1983), respectively.
121 Silicate was analysed using the procedure of Strickland and Parsons (1968).

122 Absolute and relative precision were regularly determined for reasonably high
123 concentrations in an in-house standard. For phosphate, the standard deviation was $0.028 \mu\text{M}$
124 ($N = 30$) for a concentration of $0.9 \mu\text{M}$; Hence the relative precision was 3.1%. For nitrate, the
125 values were $0.14 \mu\text{M}$ ($N = 30$) for a concentration of $14.0 \mu\text{M}$, so that the relative precision was
126 1.0%. For silicate, the values were $0.09 \mu\text{M}$ ($N = 15$) for a concentration of $21.0 \mu\text{M}$, so that
127 the relative precision was 0.4%. The detection limits were 0.007, 0.012 and $0.008 \mu\text{M}$, for
128 phosphate, nitrate and silicate, respectively.

129 For dissolved iron samples, the ultraclean “Pristine” sampling system for trace metals was
130 used (Rijkenberg et al., 2015). All bottles used for storage of reagents and samples were cleaned
131 according to an intensive three step cleaning protocol described by Middag et al. (2009).
132 Dissolved iron concentrations were measured shipboard using a Flow Injection—
133 Chemiluminescence method with preconcentration on iminodiaceticacid (IDA) resin as
134 described by De Baar et al. (2008) and modified by Klunder et al. (2011). In order to validate
135 the accuracy of the system, standard reference seawater (SAFe) was measured regularly in
136 triplicate (Johnson et al. 1997).

137 At 19 out of 32 stations a yoyo consisting of 3 to 6 casts, totaling 72 casts, of electronic
138 CTD profiles was done to monitor the temperature-salinity variability and to establish turbulent
139 mixing values from 5 to 500 m below the ocean surface. The yoyo casts were made
140 consecutively and took between 1 and 2 hours per station. They were mostly obtained in the
141 morning: at ten stations between 6 and 8 LT, at eight stations between 8 and 10 LT, and at one
142 station in the afternoon, around noon. As the observations were made in summer, the latitudinal

difference in sunrise was 1.5 h between the northernmost (earlier sunrise) and southernmost stations. This difference is taken into account and sampling times are referenced to time after local sunrise. It is assumed that the stations sampled just after sunrise more or less reflect the upper ocean conditions of (late-) nighttime cooling convection so that vertical near-homogeneity was at a maximum, and near-surface stratification at a minimum, while the late morning and afternoon stations reflected daytime stratifying near-surface conditions due to the stabilizing solar insolation.

2.1 Instrumentation and modification

A calibrated SeaBird 911plus CTD was used. The CTD data were sampled at a rate of 24 Hz, whilst lowering the instrumental package at a speed of 1 m s⁻¹. The data were processed using the standard procedures incorporated in the SBE-software, including corrections for cell thermal mass (Lueck, 1990) using the parameter setting of Mensah et al. (2009) and sensor time-alignment. All other analyses were performed using Conservative Temperature (Θ), absolute salinity SA and density anomalies σ_θ referenced to the surface using the Gibbs SeaWater-software (IOC, SCOR, IAPSO, 2010).

Observations were made with the CTD upright rather than horizontal in a lead-weighted frame without water samplers to minimize artificial turbulent overturning. Variable speeds of the flow passing the temperature and conductivity sensors will cause artificial temperature and thus apparent turbulent overturning, noticeable in near-homogeneous waters such as found near the surface during nighttime convection. To eliminate variable flow speeds, a custom-made assembly with pump in- and outlet tubes and tube-ends of exactly the same diameter was mounted to the CTD as described in van Haren and Laan (2016). This reduces frictional temperature effects of typically ± 0.5 mK due to fluctuations in pump speed of ± 0.5 m s⁻¹ when standard SBE-tubing is used (Appendix A1). The effective removal of the artificial temperature effects using the custom-made assembly is demonstrated in Fig. 2, in which surface wave action via ship motion is visible in the CTD-pressure record, but not in its temperature variations

record. For example, at station 32 the CTD was lowered in moderate sea state conditions with surface waves of maximum 2 m crest-trough. The surface waves are recorded by pressure variations as a result of ship motions (Fig. 2a). In the upper 40 m near the surface, the waters were near-homogeneous, with temperature variations well within ± 0.5 mK (Fig. 2b). The ΔT -variations did not vary with the surface wave periodicity of about 10 s. No correlation is found between data in Fig. 2b and Fig. 2a. This effective removal of ship motion in CTD-temperature data is confirmed for the entire 500 m depth-range in average spectral information (Fig. 2c-e). In the power spectra, the pressure gradient $dp/dt \sim$ CTD-velocity shows a clear peak around 0.1 cps, short for cycles per s, which correspond to a period of 10 s. Such a peak is absent in both spectra of temperature T and density anomaly referenced to the surface σ_θ . The correlation between dp/dt and T is not significantly different from zero (Fig. 2d,e). With conventional tubing and tube-ends, the surface wave variations would show in such ΔT -graph (van Haren and Laan, 2016). Without the effects of ship motions, considerably less corrections need to be applied for turbulence calculations (see below).

2.2 Ocean turbulence calculation

Turbulence is quantified using the analysis method by Thorpe (1977) on density (ρ) inversions of less dense water below a layer of denser water in a vertical (z) profile. Such inversions are interpreted as turbulent overturns of mechanical energy mixing. Vertical turbulent kinetic energy dissipation rate (ε) is a measure of the amount of kinetic energy put in a system for turbulent mixing. It is proportional to turbulent diapycnal flux (of density) $K_z dp/dz$. In practice it is determined by calculating overturning scales with magnitude $|d|$, just like turbulent eddy diffusivity (K_z). The vertical density stratification is indicated by dp/dz . The turbulent overturning scales are obtained after reordering the potential density profile $\sigma_\theta(z)$, which may contain inversions, into a stable monotonic profile $\sigma_\theta(z_s)$ without inversions (Thorpe, 1977). After comparing raw and reordered profiles, displacements $d = \min(|z - z_s|) \cdot \text{sgn}(z - z_s)$ are calculated that generate the stable profile. Then,

$$\varepsilon = 0.64d^2N^3 \quad [\text{m}^2\text{s}^{-3}], \quad (1)$$

where $N = \{-g/\rho(dp/dz + gp/c_s^2)\}^{1/2}$ (e.g., Gill, 1982) denotes the buoyancy frequency (\sim square-root of stratification as is clear from the equation) computed from the reordered profile. Here, g is the acceleration of gravity and c_s the speed of sound reflecting pressure-compressibility effects. N is computed over a typical vertical length-scale of $\Delta z = 100$ m, which more or less represents the scale of large internal waves that are supported by the density stratification. The numerical constant of 0.64 in (1) follows from empirically relating the overturning scale magnitude with the Ozmidov scale L_O of largest possible turbulent overturn in a stratified flow: $(L_O/|d|)_{\text{rms}} = 0.8$ (Dillon, 1982), a mean coefficient value from many realizations. Using $K_z = \Gamma \varepsilon N^{-2}$ and a mean mixing efficiency coefficient of $\Gamma = 0.2$ for the conversion of kinetic into potential energy for ocean observations that are suitably averaged over all relevant turbulent overturning scales of the mix of shear-, current differences, and convective, buoyancy driven, turbulent overturning in large Reynolds number flow conditions (e.g., Osborn, 1980; Oakey, 1982; Ferron et al., 1998; Gregg et al., 2018), we find,

$$K_z = 0.128d^2N \quad [\text{m}^2\text{s}^{-1}]. \quad (2)$$

This parametrization is also valid for the upper ocean, as has been shown extensively by Oakey (1982) and recently confirmed by Gregg et al. (2019). The inference is that the upper ocean may be weakly stratified at times, but stratification and turbulence vary considerably with time and space. Sufficient averaging collapses coefficients to the mean values given above. This is confirmed in recent numerical modeling by Portwood et al. (2019).

As K_z is a mechanical turbulence coefficient it is not property-dependent like a molecular diffusion coefficient that is about 100-fold different for temperature compared to salinity. K_z is thus the same for all turbulent transport calculations no matter what gradient of what property. For example, the vertical turbulent flux of dissolved iron is computed as $K_z d(\text{DFe})/dz$.

According to Thorpe (1977), results from (1) and (2) are only useful after averaging over the size of a turbulent overturn instead of using single displacements. Here, root-mean-square-displacement values d_{rms} are not determined over individual overturns, as in Dillon (1982), but over 7 m vertical intervals (equivalent to about 200 raw data samples) that just exceed average

Lo. This avoids the complex distinction of smaller overturns in larger ones and allows the use of a single length scale of averaging. As a criterion for determining overturns we only used those data of which the absolute value of difference with the local reordered value exceeds a threshold of $7 \times 10^{-5} \text{ kg m}^{-3}$, which corresponds to applying a threshold of $1.4 \times 10^{-3} \text{ kg m}^{-3}$ to raw data variations (e.g., Galbraith and Kelley, 1996; Stansfield et al., 2001; Gargett and Garner, 2008). Vertically averaged turbulence values, short for averaged ϵ - and K_z -values from (1) and (2), can be calculated to within an error of a factor of two to three, approximately. As will be demonstrated below, this is considerably less spread in values than the natural turbulence values variability over typically four orders of magnitude at a given position and depth in the ocean (e.g., Gregg, 1989).

3 Results

3.1 Physical parameters

An early morning vertical profile of density anomaly in the upper 500 m at a northern station (Fig. 3a) is characterized by a near-homogeneous layer of about 15 to 40 m, which is above a layer of relatively strong stratification and a smooth moderate stratification deeper below. In the near-homogeneous upper layer, in this example $z > -30 \text{ m}$, relatively large turbulent overturn displacements can be found of $d = \pm 20 \text{ m}$ (Fig. 3b): so called large density inversions. For $-200 < z < -30 \text{ m}$, large turbulent overturns are few and far between. Turbulence dissipation rate (Fig. 3c) and eddy diffusivity (Fig. 3d) are characterized by relatively small displacement sizes of less than 5 m. For $z < -200 \text{ m}$, displacement values weakly increase with depth, together with stratification ($\sim N^2$; Fig. 3e). Between $-30 < z < 0 \text{ m}$, turbulence dissipation rate values between $< 10^{-11}$ and $> 10^{-8} \text{ m}^2 \text{ s}^{-3}$ are similar to those found by others, using microstructure profilers (e.g., Oakey, 1982; Gregg, 1989), lowered acoustic Doppler current profiler or CTD-Thorpe scale analysis (e.g., Ferron et al., 1998; Walter et al., 2005; Kunze et al., 2006). Here, eddy diffusivities are found between $< 10^{-5}$ and $3 \times 10^{-3} \text{ m}^2 \text{ s}^{-1}$ and these values compare with previous near-surface results (Denman and Gargett, 1983). The relatively small

$|d| < 5$ m displacements (Fig. 3b) are genuine turbulent overturns, and they resemble ‘Rankine vortices’, a common model of cyclones (van Haren and Gostiaux, 2014), as may be best visible in this example in the large turbulent overturn near the surface. The occasional erratic appearance in individual profiles, sometimes still visible in the ten-profile means, reflects smaller overturns in larger ones.

A mid-morning profile at a southern station shows different characteristics (Fig. 4), although 500 m vertically averaged turbulence values are similar to within 10% of those of the northern station. This 10% variation is well within the error bounds of about a factor of two. At this southern station, the near-surface layer is stably stratifying (Fig. 4a) and displays few overturning displacements (Fig. 4b), while the interior demonstrates rarer but occasional intense turbulent overturning (at $z = -160$ m in Fig. 4), presumably due to internal wave breaking. At greater depths, stratification ($\sim N^2$; Fig. 4e) weakly decreases, together with ϵ (Fig. 4c) and K_z (Fig. 4d).

Latitudinal overviews are given in Fig. 5 for: Average values over the upper $z > -15$ m, which covers the diurnal mainly convective turbulent mixing range from the surface, average values between $-100 < z < -25$ m, which covers the seasonal strong stratification, and average values between $-500 < z < -100$ m, which covers the more permanent moderate stratification. Noting that all panels have a vertical axis representing a logarithmic scale, variations over nearly four orders of magnitude in turbulence dissipation rate (Fig. 5a) and eddy diffusivity (Fig. 5b) are observed between casts at the same station. This variation in magnitude is typically found in near-surface open-ocean turbulence microstructure profiles (e.g., Oakey, 1982). Still, considerable variability over about two orders of magnitude is observed between the averages from the different stations. This variation in station- and vertical averages far exceeds the instrumental error bounds of a factor of two (0.3 on a log-scale), and thus reveals local variability. The turbulence processes occur ‘intermittently’.

The observed variability over two orders of magnitude between yoyo-casts at a single station may be due to active convective overturning during early morning in the near-homogeneous upper layer, or due to internal wave breaking and sub-mesoscale variability

deeper down. Despite the large variability at stations, trends are visible between stations in the upper 100 m over the 32° latitudinal range going poleward: Buoyancy frequency (\sim square root of stratification) steadily decreases significantly (p -value < 0.05) given the spread of values at given stations, while turbulence values vary insignificantly with latitude as they remain the same or weakly increase by about half an order of magnitude (about a factor of 3). At a given depth range, turbulence dissipation rate roughly follow a log-normal distribution with standard deviations well exceeding half an order of magnitude. The comparison of latitudinal variations with the (log-normal) distribution are declared insignificant with $p > 0.05$ when the mean values are found within 2 standard deviations (see Appendix A2). This is not only performed for turbulence dissipation rate, but also for other quantities. The trends suggest only marginally larger turbulence going poleward, which is possibly due to larger cooling from above and larger internal wave breaking deeper down. It is noted that the results are somewhat biased by the sampling scheme, which changed from 3 to 4 h after sunrise sampling at high latitudes to 4 to 5 h after sunrise sampling at lower latitudes, see the sampling hours after local sunrise in (Fig. 5d). Its effect is difficult to quantify, but should not show up in turbulence values from deeper down ($-500 < z < -100$ m).

Between $-500 < z < -100$ m, no clear significant trend with latitude is visible in the turbulence values (Fig. 5a,b), although $[K_z]$ weakly increases with increasing latitude at all levels between $-500 < z < 0$ m, while buoyancy frequency significantly decreases (Fig. 5c). The data from well-stratified waters deeper down thus show the same latitudinal trend as the observations from the near-surface layers. Our turbulence values from CTD-data also confirm previous results by Jurado et al. (2012) who made microstructure profiler observations from the upper $z > -100$ m along the same transect. Their results showed turbulence values remain unchanged over 30° latitude or increase by at most one order of magnitude, depending on depth level. Their ‘mixed’ layer ($z > \sim -25$ m) turbulence values are similar to our $z > -15$ m values and half to one order of magnitude larger than the present deeper observations. The slight discrepancy in values averaged over $z > -25$ m may point at either i) a low bias due to a too strict criterion of accepting density variations for reordering applied here, or ii) a high bias of

the ~10-m largest overturns having similar velocity scales (of about 0.05 m s^{-1}) as their 0.1 m s^{-1} slowly descending SCAMP microstructure profiler. At greater depths, $-500 < z < -100 \text{ m}$, it is seen in the present observations that the spread in turbulence values over four orders of magnitude at a particular station is also large. This spread in values suggests that dominant turbulence processes show similar intermittency in weakly (at high-latitudes $N \approx 10^{-2.5} \text{ s}^{-1}$) and moderately (at mid-latitudes $N \approx 10^{-2.2} \text{ s}^{-1}$) stratified waters, respectively, for given resolution of the instrumentation.

Mean values of N are larger by half an order of magnitude in the seasonal pycnocline than those near the surface and in the more permanent stratification below (Fig. 5). Such local vertical variations in N have the same range of variation as observed horizontally across latitudes $[30, 62]^\circ$ per depth level.

3.2 Nutrient distributions and fluxes

Vertical profiles of macro-nutrients generally resemble those of density anomaly in the upper $z > -500 \text{ m}$ (Fig. 6). In the south, low macro-nutrient values are generally distributed over a somewhat larger near-surface mixed layer. The mixed layer depth, defined as the depth at which the temperature difference with respect to the surface was 0.5°C (Jurado et al., 2012), varies between about 20 and 30 m on the southern end of the transect and weakly becomes shallower with latitude (Fig. 7a). This weak trend may be expected from the summertime wind conditions that also barely vary with latitude (Fig. 7b,c). In contrast, the euphotic zone, defined as the depth of the 0.1% irradiance penetration level (Mojica et al., 2015), demonstrates a clear latitudinal trend decreasing from about 150 to 50 m (Fig. 7a). For $z < -100 \text{ m}$ below the seasonal stratification, vertical gradients of macro-nutrients are large (Fig. 6b-d). Macro-nutrient values become more or less independent of latitude at depths below $z < -500 \text{ m}$. Dissolved iron profiles differ from macro-nutrient profiles, notably in the upper layer near the surface (Fig. 6a). At some southern stations, dissolved iron and to a lesser extent also phosphate, have relatively high concentrations closest to the surface. These near-surface concentration increases suggest atmospheric sources, most likely Saharan dust deposition (e.g., Rijkenberg et al., 2012).

As a function of latitude in the near-surface ‘mixed’ layer (Fig. 8), the vertical turbulent fluxes of dissolved iron and phosphate (representing the macro-nutrients, for graphical reasons, see the similarity in profiles in Fig.6b-d) are found constant or insignificantly ($p > 0.05$) increasing (Fig. 8d). Here, the mean eddy diffusivity values for the near-surface layer as presented in Fig. 5 are used for computing the fluxes. It is noted that in this layer turbulent overturning (Figs 3b, 4b) is larger and nutrients are mainly depleted (Fig. 6), except when replenished from atmospheric sources. Hereby, lateral diffusion is not considered important. More interestingly, the vertical turbulent fluxes of nutrients across the seasonal pycnocline (Fig. 9) are found ambiguous or statistically independently varying with latitude (Fig. 9d). Likewise, the vertical turbulent fluxes of dissolved iron and phosphate are marginally constant with latitude across the more permanent stratification (Fig. 10). Nitrate fluxes show the same latitudinal trend, with values around $10^{-6} \text{ mmol m}^{-2} \text{ s}^{-1}$. Such values are of the same order of magnitude as reported for the interior of the Saint Lawrence seaway (Cyr et al., 2015). Overall, the vertical turbulent nutrient fluxes across the seasonal and more permanent stratification resemble those of the physical vertical turbulent mass flux, which is equivalent to the distribution of turbulence dissipation rate and which is latitude-invariant (Fig. 5a).

4 Discussion

Practically, the upright positioning CTD while using an adaptation consisting of a custom-made equal-surface inlet worked well to minimize ship-motion effects on variable flow-imposed temperature variations. This improved calculated turbulence values from CTD-observations in general and in near-homogeneous layers in particular. The indirect comparison with previous microstructure profiler observations along the same transect (Jurado et al., 2012) confirms the same trends, although occasionally turbulence values were lower (to one order of magnitude in the present study). This difference in values may be due to the time lapse of 8 years between the observations, but more likely it is due to inaccuracies in one or both methods. It is noted that any ocean turbulence observations cannot be made better than to within a factor

of two (Oakey, pers. comm.). In that respect, the standard CTD with the here presented adaptation is a cheaper solution than additional microstructure profiler observations. Although the general understanding, mainly amongst modellers, is that the Thorpe length method overestimates diffusivity (e.g., Scotti, 2015; Mater and Venayagamoorthy, 2015), this view is not shared amongst ocean observers (e.g., Gregg et al., 2018). In the large parameter space of the high Reynolds number environment of the ocean, turbulence properties vary constantly, with an interminglement of convection and shear-induced turbulence at various levels. Given sufficient averaging, and adequate mean value parametrization, the Thorpe length method is not observed to overestimate diffusivity. This property of adequate and sufficient averaging yields similar mean parameter values in recent modelling results estimating a mixing coefficient near the classical bound of 0.2 in stationary flows for a wide range of conditions (Portwood et al., 2019). It is noted that diffusivity always requires knowledge of stratification to obtain a turbulent flux, and it is better to consider turbulence dissipation rate for intercomparison purposes. Nevertheless, future research may perform a more extensive comparison between Thorpe scale analysis data and deeper microstructure profiler data.

While our turbulence values are roughly similar to those of others transecting the NE-Atlantic over the entire water depth (Walter et al., 2005; Kunze et al., 2006), the focus in the present paper is on the upper 500 m because of its importance for upper-ocean marine biology. Our study demonstrates a significant decrease of stratification with increasing latitude and decreasing temperature that, however, does not lead to significant variation in turbulence values and vertical turbulent fluxes. These findings can suggest that global warming may not necessarily lead to a change in vertical turbulent exchange. We hypothesize that internal waves may drive the feed-back mechanism, participating in the subtle balance between destabilizing shear and stable (re)stratification as outlined below.

Molecular diffusivity of heat is about $10^{-7} \text{ m}^2 \text{ s}^{-1}$ in seawater, and nearly always smaller than turbulent diffusivity in the ocean. The average values of K_z during our study were typically 100 to 1000 times larger than molecular diffusivity, which implies turbulent diapycnal mixing drives vertical fluxes despite the relatively slow turbulence compared to surface wave breaking.

Depending on the gradient of a substance like nutrients or matter, the relatively slow turbulence may not necessarily provide weak fluxes $K_z d(\text{substance})/dz$ into the photic zone. In the central North Sea, a relatively low mean value of $K_z = 2 \times 10^{-5} \text{ m}^2 \text{ s}^{-1}$ comparable to values over the seasonal pycnocline here, was found sufficient to supply nutrients across the strong summer pycnocline to sustain the entire late-summer phytoplankton bloom in near-surface waters and to warm up the near-bottom waters by some 3°C over the period of seasonal stratification (van Haren et al., 1999). There, the turbulent exchange was driven by a combination of tidal currents modified by the stratification, shear by inertial motions driven by the Coriolis force (inertial shear) and internal wave breaking. Such drivers are also known to occur in the open ocean, although to unknown extent.

The here observed (lack of) latitudinal trends of ε , K_z and N yield more or less the same information as the vertical trends in these parameters at all stations. In the vertical for $z < -200$ m, turbulence values of ε and K_z weakly vary with stratification. This is perhaps unexpected and contrary to the common belief of stratification hampering vertical turbulent exchange of matter including nutrients. It is less surprising when considering that increasing stratification is able to support larger shear. Known sources of destabilizing shear include near-inertial internal waves of which the vertical length-scale is relatively small compared to other internal waves, including internal tides (LeBlond and Mysak, 1978).

The dominance of inertial shear over shear by internal tidal motions (internal tide shear), together with larger energy in the internal tidal waves, has been observed in the open-ocean, e.g. in the Irminger Sea around 60°N (van Haren, 2007). The frequent atmospheric disturbances in that area generate inertial motions and dominant inertial shear. Internal tides have larger amplitudes but due to much larger length scales they generate weaker shear, than inertial motions. Small-scale internal waves near the buoyancy frequency are abundant and may break sparsely in the ocean interior outside regions of topographic influence. However, larger destabilizing shear requires larger stable stratification to attain a subtle balance of ‘constant’ marginal stability (van Haren et al., 1999). Not only storms, but other geostrophic adjustments, such as frontal collapse, may generate inertial wave shear also at low latitudes (Alford and

Gregg, 2001), so that overall latitudinal dependence may be negligible. If shear-induced turbulence in the upper ocean is dominant it may thus be latitudinally independent (Jurado et al., 2012; deeper observations present study). There are no indications that the overall open ocean internal wave field and (sub)mesoscale activities are energetically much different across the mid-latitudes.

Summarizing, our data imply that vertical nutrient fluxes did not vary with latitude and stratification and thus from a physical environment perspective, nutrient availability and corresponding summer phytoplankton productivity and growth are not expected to change under future environmental changes like global warming. We invite future observations and numerical modelling to further investigate this suggestion and associated feed-back mechanisms such as internal wave breaking.

Competing interests. The authors declare that they have no conflict of interest.

Acknowledgements. We thank the master and crew of the R/V Pelagia for their pleasant contributions to the sea-operations. J. van Heerwaarden and R. Bakker made the CTD-modification.

Modification of CTD pump-tubing to minimize RAM-effects

The unique pump system on SeaBird Electronics (SBE) CTDs, foremost on their high-precision full ocean depth shipborne and cable-lowered SBE911, minimizes the effects of flow variations (and inversions) past its T-C sensors (SeaBird, 2012). This reduction in flow variation is important, because the T-sensor has a slower response than the C-sensor. As data from the latter are highly temperature dependent, besides being pressure dependent, the precise matching of all three sensors is crucial for establishing proper salinity and density measurements, especially across rapid changes in any of the parameters. As flow past the T-sensor causes higher measurement values due to friction at the sensor tip, flow-fluctuations are to be avoided as they create artificial T-variations of about 1 mK s m^{-1} (Larson and Pedersen, 1996).

However, while the pump itself is one thing, its tubing needs careful mounting as well, with in- and outlet at the same depth level (Sea-Bird, 2012). This is to prevent ram pressure $P = \rho U^2$, for density ρ and flow speed U . Unfortunately, the SBE-manual shows tubing of different diameter, for in- and outlet. Different diameter tubing leads to velocity fluctuations of $\pm 0.5 \text{ m s}^{-1}$ past the T-sensor, as was concluded from a simple experiment by van Haren and Laan (2016). The flow speed variations induce temperature variations of $\pm 0.5 \text{ mK}$ and are mainly detectable in weakly stratified waters such as in the deep ocean, but also near the surface as observed in the present data. Using tubes of the same diameter opening remedied most of the effect, but only if the surface of the tube-opening is perpendicular to the main CT-motion as in a vertically mounted CTD. If it is parallel to the main motion as in a horizontally mounted CTD, the effect was found to be adverse. The make-shift onboard experiment in van Haren and Laan (2016) has now been cast into a better design (Fig. A1), of which the first results are presented in this paper.

PDFs of vertically averaged dissipation rate in comparison with latitudinal trends

Ocean turbulence dissipation rate generally tends to a nearly log-normal distribution (e.g., Pearson and Fox-Kemper, 2018), so that the probability density function (PDF) of the logarithm of ε -values is normally distributed and can be described by the first two moments, the mean and its standard deviation. It is seen in Fig. A2a that the overall distribution of all present data indeed approaches lognormality, despite the relatively large length-scale used in the computations (cf., Yamazaki and Lueck, 1990). When the data are split in the three depth levels as in Fig. 5a, it is seen that ε in the upper $z > -15$ m layer is not log-normally distributed due to a few outlying high values confirming an ocean state dominated by a few turbulence bursts (Moum and Rippeth, 2009), whereas ε in the deeper more stratified layers is nearly log-normally distributed.

When we compare the mean and standard deviations of the distributions with the extreme values of the latitudinal trends as computed for Fig. 5a it is seen that for none of the three depth levels the extreme values are found outside one standard deviation from the mean value. In fact, for deeper stratified waters the extreme values of the trends are found very close to the mean value. It is concluded that the mean dissipation rate does not show a significant trend with latitude, at all depth levels. The same exercise yields extreme buoyancy frequency values lying outside one standard deviation from the mean values for well-stratified waters, from which we conclude that stratification significantly decreases with latitude. This is inferable from Fig. 5c by investigating the spread of mean values around the trend line.

References

- Alford, M. H. and Gregg, M. C.: Near-inertial mixing: Modulation of shear, strain and microstructure at low latitude, *J. Geophys. Res.*, 106, 16,947-16,968, 2001.
- Charria, G., Theetten, S., Vandermeirsch, F., Yelekçi, Ö and Audiffren, N.: Interannual evolution of (sub)mesoscale dynamics in the Bay of Biscay, *Ocean Sci.*, 13, 777-797, 2017.
- Cyr, F., Bourgault, D., Galbraith, P. S. and Gosselin, M.: Turbulent nitrate fluxes in the Lower St. Lawrence Estuary, Canada, *J. Geophys. Res.*, 120, 2308-2330, doi:10.1002/2014JC010272, 2015.
- De Baar, H. J. W. et al.: Titan: A new facility for ultraclean sampling of trace elements and isotopes in the deep oceans in the international Geotraces program, *Mar. Chem.*, 111, 4-21, 2008.
- Denman, K. L. and Gargett, A. E.: Time and space scales of vertical mixing and advection of phytoplankton in the upper ocean, *Limnol. Oceanogr.*, 28, 801-815, 1983.
- Dillon, T. M.: Vertical overturns: A comparison of Thorpe and Ozmidov length scales, *J. Geophys. Res.*, 87, 9601-9613, 1982.
- Ferron, B., Mercier, H., Speer, K., Gargett, A. and Polzin, K.: Mixing in the Romanche Fracture Zone, *J. Phys. Oceanogr.*, 28, 1929-1945, 1998.
- Galbraith, P. S. and Kelley, D. E.: Identifying overturns in CTD profiles, *J. Atmos. Oc. Technol.*, 13, 688-702, 1996.
- Gargett, A. and Garner, T.: Determining Thorpe scales from ship-lowered CTD density profiles, *J. Atmos. Oc. Technol.*, 25, 1657-1670, 2008.
- Gill, A. E.: *Atmosphere-Ocean Dynamics*, Academic Press, Orlando, FL, USA, 662 pp, 1982.
- Grasshoff, K., Kremling, K. and Ehrhardt, M.: *Methods of seawater analysis*, Verlag Chemie GmbH, Weinheim, 419 pp, 1983.
- Gregg, M. C.: Scaling turbulent dissipation in the thermocline, *J. Geophys. Res.*, 94, 9686-9698, 1989.

Gregg, M. C., D'Asaro, E. A., Riley, J. J. and Kunze, E.: Mixing efficiency in the ocean, *Ann. Rev. Mar. Sci.*, 10, 443-473, 2018.

Hernández-Hernández, N. et al.: Drivers of plankton distribution across mesoscale eddies at submesoscale range, *Front. Mar. Sci.*, 7, 667, doi:10.3389/fmars.2020.00667, 2020.

Huisman, J., Pham Thi, N. N., Karl, D. M. and Sommeijer, B.: Reduced mixing generates oscillations and chaos in the oceanic deep chlorophyll maximum, *Nature*, 439, 322-325, 2006.

Jurado, E., van der Woerd, H. J. and Dijkstra, H. A.: Microstructure measurements along a quasi-meridional transect in the northeastern Atlantic Ocean, *J. Geophys. Res.*, 117, C04016, doi:10.1029/2011JC07137, 2012.

IOC, SCOR, IAPSO: The international thermodynamic equation of seawater – 2010: Calculation and use of thermodynamic properties, Intergovernmental Oceanographic Commission, Manuals and Guides No. 56, UNESCO, Paris, France, 196 pp, 2010.

Johnson, K. S., Gordon, R. M. and Coale, K. H.: What controls dissolved iron concentrations in the world ocean? *Mar. Chem.*, 57, 137-161, 1997.

Klunder, M. B., Laan, P., Middag, R., De Baar, H. J. W. and van Ooijen, J. C.: Dissolved iron in the Southern Ocean (Atlantic sector), *Deep-Sea Res. II*, 58, 2678-2694, 2011.

Kunze, E., Firing, E., Hummon, J. M., Chereskin, T. K. and Thurnherr, A. M.: Global abyssal mixing inferred from lowered ADCP shear and CTD strain profiles, *J. Phys. Oceanogr.* 36, 1553-1576, 2006.

Larson, N., Pedersen, A. M.: Temperature measurements in flowing water: viscous heating of sensor tips, *Proc. 1st IGHEM Meeting*, Montreal, PQ, Canada. [Available online at http://www.seabird.com/technical_references/viscous.htm], 1996.

LeBlond, P. H. and Mysak, L. A.: *Waves in the Ocean*, Elsevier, Amsterdam NL, 602 pp, 1978.

Lueck, R. G.: Thermal inertia of conductivity cells: Theory, *J. Atmos. Oc. Technol.*, 7, 741-755, 1990.

Mater, B. D., Venayagamoorthy, S. K., St. Laurent, L. and Moum, J. N.: Biases in Thorpe-scale estimates of turbulence dissipation. Part I: Assessments from largescale overturns in oceanographic data, *J. Phys. Oceanogr.*, 45, 2497-2521, 2015.

Mensah, V., Le Menn, M. and Morel, Y.: Thermal mass correction for the evaluation of salinity, *J. Atmos. Oc. Tech.*, 26, 665-672, 2009.

Middag, R., de Baar, H. J. W., Laan, P. and Bakker, K.: Dissolved aluminium and the silicon cycle in the Arctic Ocean, *Marine Chemistry*, 115, 176-195, 2009.

Mojica, K. D. A. et al.: Phytoplankton community structure in relation to vertical stratification along a north-south gradient in the Northeast Atlantic Ocean, *Limnol. Oceanogr.*, 60, 1498-1521, 2015.

Mojica, K. D. A., Huisman, J., Wilhelm, S. W. and Brussaard, C. P. D.: Latitudinal variation in virus-induced mortality of phytoplankton across the North Atlantic Ocean, *ISME J.*, 10, 500-513, 2016.

Moum, J. N. and Rippeth, T. P.: Do observations adequately resolve the natural variability of oceanic turbulence?, *J. Mar. Sys.*, 77, 409-417, 2009.

Murphy, J. and Riley, J. P.: A modified single solution method for the determination of phosphate in natural waters, *Anal. Chim. Acta*, 27, 31-36, 1962.

Oakey, N. S.: Determination of the rate of dissipation of turbulent energy from simultaneous temperature and velocity shear microstructure measurements, *J. Phys. Oceanogr.*, 12, 256-271, 1982.

Osborn, T. R.: Estimates of the local rate of vertical diffusion from dissipation measurements, *J. Phys. Oceanogr.*, 10, 83-89, 1980.

Pearson, B. and Fox-Kemper, B.: Log-normal turbulence dissipation in global ocean models, *Phys. Rev. Lett.*, 120, 094501, 2018.

Portwood, G. D., de Bruyn Kops, S. M. and Caulfield, C. P.: Asymptotic dynamics of high dynamic range stratified turbulence, *Phys. Rev. Lett.*, 122, 194504, 2019.

Rijkenberg, M. J. A. et al.: Fluxes and distribution of dissolved iron in the eastern (sub-) tropical North Atlantic Ocean, *Glob. Biogeochem. Cycl.*, 26, GB3004, doi:10.1029/2011GB004264, 2012.

Rijkenberg, M. J. A. et al.: “PRISTINE”, a new high volume sampler for ultraclean sampling of trace metals and isotopes, *Mar. Chem.*, 177, 501-509, 2015.

Sarmiento, J. L. et al.: Response of ocean ecosystems to climate warming, *Glob. Biogeochem. Cycl.*, 18, doi:10.1029/2003GB002134, 2004.

Scotti, A.: Biases in Thorpe-scale estimates of turbulence dissipation. Part II: energetics arguments and turbulence simulations, *J. Phys. Oceanogr.*, 45, 2522-2543, 2015.

Sea-Bird: Fundamentals of the TC duct and pump-controlled flow used on Sea-Bird CTDs, *Proc. Sea-Bird Electronics Appl. note 38*, SBE, Bellevue, WA, USA, 5 pp, 2012.

Smith, W. H. F. and Sandwell, D. T. : Global seafloor topography from satellite altimetry and ship depth soundings, *Science* 277, 1957-1962, 1997.

Stansfield, K., Garrett, C., Dewey, R.: The probability distribution of the Thorpe displacement within overturns in Juan de Fuca Strait, *J. Phys. Oceanogr.*, 31, 3421-3434, 2001.

Strickland, J. D. H. and Parsons, T. R.: A practical handbook of seawater analysis, First edition, Fisheries Research Board of Canada, Bulletin, 167, 293 pp, 1968.

Thorpe, S. A.: Turbulence and mixing in a Scottish loch, *Phil. Trans. Roy. Soc. Lond. A*, 286, 125-181, 1977.

van Haren, H.: Tidal and near-inertial peak variations around the diurnal critical latitude, *Geophys. Res. Lett.*, 32, L23611, doi:10.1029/2005GL024160, 2005.

van Haren, H.: Inertial and tidal shear variability above Reykjanes Ridge, *Deep-Sea Res. I*, 54, 856-870, 2007.

van Haren, H. and Gostiaux, L.: Characterizing turbulent overturns in CTD-data, *Dyn. Atmos. Oc.*, 66, 58-76, 2014.

- 587 van Haren, H. and Laan, M.: An in-situ experiment identifying flow effects on temperature
588 measurements using a pumped CTD in weakly stratified waters, *Deep-Sea Res. I*, 111, 11-
589 15, 2016.
- 590 van Haren, H., Maas, L., Zimmerman, J. T. F., Ridderinkhof, H. and Malschaert, H.: Strong
591 inertial currents and marginal internal wave stability in the central North Sea, *Geophys.*
592 *Res. Lett.*, 26, 2993-2996, 1999.
- 593 Walter, M., Mertens, C. and Rhein, M.: Mixing estimates from a large-scale hydrographic
594 survey in the North Atlantic, *Geophys. Res. Lett.*, 32, L13605, doi:10.1029/2005GL022471,
595 2005.
- 596 Yamazaki, H. and Lueck, R.: Why oceanic dissipation rates are not lognormal, *J. Phys.*
597 *Oceanogr.*, 20, 1907-1918, 1990.

Figure 1. Bathymetry map of the Northeast Atlantic Ocean based on the 9.1 ETOPO-1 version of satellite altimetry-derived data by Smith and Sandwell (1997). The numbered circles indicate the CTD stations. Depth contours are at 2500 and 5000 m.

Figure 2. Test of effective removal of ship motions in CTD-data after pump in- and outlet modification. Nearly raw 24 Hz sampled downcast data obtained from northern station 32 (cast 9). Short example time series for the 20-m depth range [10, 30] m. (a) Detrended pressure (blue) and its (negative signed) first time derivative $-dp/dt$, 2-dbar-smoothed (purple). (b) Detrended temperature. (c) Moderately smoothed (~ 30 degrees of freedom; dof) spectra of data from the 5 to 500 m depth range. (d) Moderately smoothed (40 dof) coherence between dp/dt and T from c., with dashed line indicating the 95% significance level. (e) Corresponding phase difference.

Figure 3. Upper 500 m of turbulence characteristics computed from downcast density anomaly data applying a threshold of $7 \times 10^{-5} \text{ kg m}^{-3}$. Northern station 29, cast 2. (a) Unordered, ‘raw’ profile of density anomaly referenced to the surface. (b) Overturn displacements following reordering of the profiles in a. Slopes $\frac{1}{2}$ (solid lines) and 1 (dashed lines) are indicated. (c) Logarithm of dissipation rate computed from the profiles in a., averaged over 7 m intervals. (d) As c., but for eddy diffusivity. (e) Logarithm of buoyancy frequency computed after reordering the profiles of a.

Figure 4. As Fig. 3, but for a southern station. Upper 500 m of turbulence characteristics computed from downcast density anomaly data applying a threshold of $7 \times 10^{-5} \text{ kg m}^{-3}$. Southern station 3, cast 4. (a) Unordered, ‘raw’ profile of density anomaly referenced to the surface. (b) Overturn displacements following reordering of the profiles in a. Slopes $\frac{1}{2}$ (solid lines) and 1 (dashed lines) are indicated. (c) Logarithm of dissipation rate computed from the profiles in a., averaged over 7 m intervals. (d) As c., but for eddy diffusivity. (e) Logarithm of buoyancy frequency computed after reordering the profiles of a.

Figure 5. Summer 2017 latitudinal transect along $17\pm5^\circ\text{W}$ of turbulence values for upper 15 m averages (green) and averages between $-100 < z < -25$ m (blue, seasonal pycnocline) and $500 < z < -100$ m (black, more permanent pycnocline) from short yoyos of 3 to 6 CTD-casts. Values are given per cast (o) and station average (heavy circle with x; the size corresponds with \pm the standard error for turbulence parameters). (a) Logarithm of dissipation rate. (b) Logarithm of diffusivity. (c) Logarithm of buoyancy frequency (the small symbols have the size of \pm the standard error). (d) Hour of sampling after sunrise.

Figure 6. Upper 500 m profiles for stations at three latitudes. (a) Density anomaly referenced to the surface, including profiles from Fig. 3a and 4a. (b) Nitrate plus nitrite. (c) Phosphate. (d) Silicate. (e) Dissolved iron.

Figure 7. Latitudinal transect of near-surface layers and wind conditions measured at stations during the observational survey. (a) Mixed layer depth (x) and euphotic zone (o). (b) Wind speed. (c) Wind direction.

Figure 8. Latitudinal transect of near-surface nutrient concentrations. (a) Dissolved iron. (b) Nitrate plus nitrite (red) and phosphate (blue, scale times 10). (c) Logarithm of vertical gradients of values dissolved iron in a. and phosphate in b. (d). Vertical turbulent fluxes of concentrations in c. using average surface K_z from Fig. 5c.

Figure 9. As Fig. 8, but for $-100 < z < -25$ m.

Figure 10. As Fig. 8, but for -600 (few nutrients sampled at 500) $< z < -100$ m.

Fig. A1. SBE911 CTD-pump in- and outlet modification following the findings in van Haren and Laan (2016). (a) The T- and C-sensors clamped together with a structure holding in-

and outlet pump-tubing of exactly the same diameter, separated at 0.3 m distance in the horizontal plane. (b) The modification of a. mounted in the CTD-frame.

Fig. A2. Probability Density Functions of logarithm of vertically averaged dissipation rate in comparison with latitudinal trend extreme values. (a) Distribution as a function of latitude for all data. (b) As a, but for the upper 15 m averages only. The mean value is given by the vertical purple line, with the horizontal line indicating +/- 1 standard deviation. The vertical light-blue lines indicate the best-fit value of the trend for 30° and 63°N. (c) As b, but for averages between $-100 < z < -25$ m. (d) As c, but for averages between $-500 < z < -100$ m.

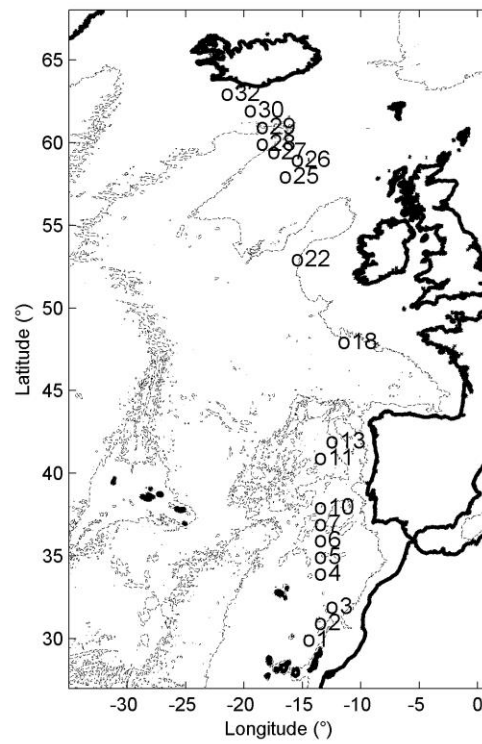


Figure 1. Bathymetry map of the Northeast Atlantic Ocean based on the 9.1 ETOPO-1 version of satellite altimetry-derived data by Smith and Sandwell (1997). The numbered circles indicate the CTD stations. Depth contours are at 2500 and 5000 m.

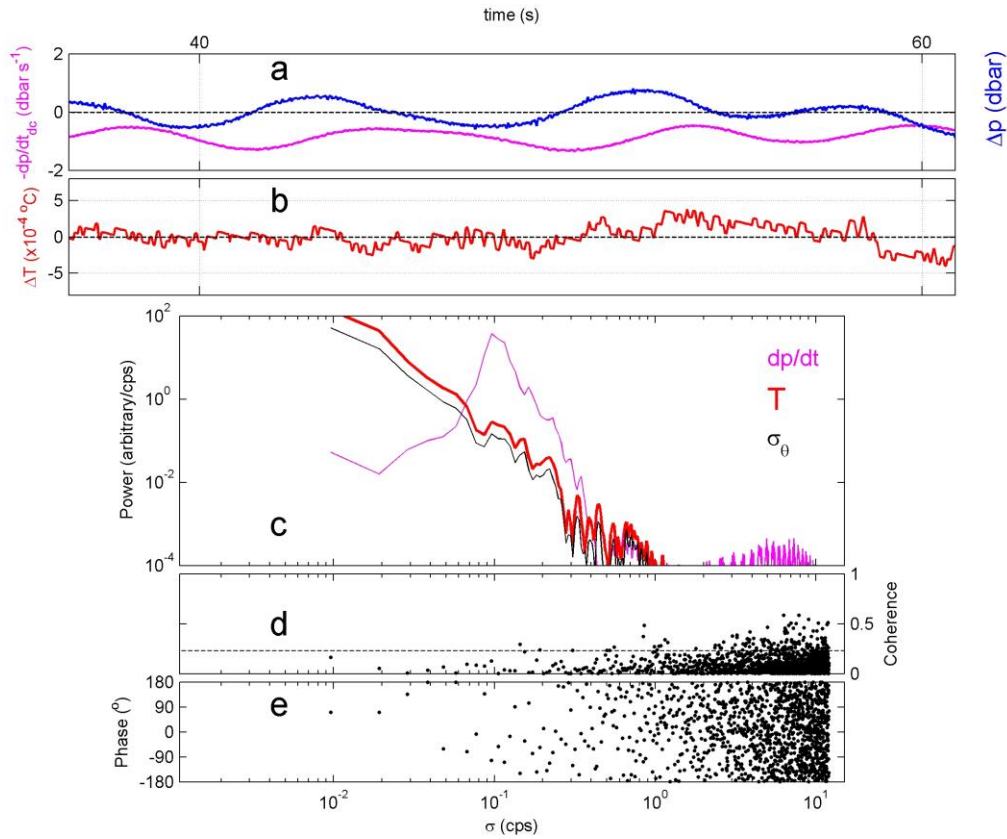


Figure 2. Test of effective removal of ship motions in CTD-data after pump in- and outlet modification. Nearly raw 24 Hz sampled downcast data obtained from northern station 32 (cast 9). Short example time series for the 20-m depth range [10, 30] m. (a) Detrended pressure (blue) and its (negative signed) first time derivative $-dp/dt$, 2-dbar-smoothed (purple). (b) Detrended temperature. (c) Moderately smoothed (~ 30 degrees of freedom; dof) spectra of data from the 5 to 500 m depth range. (d) Moderately smoothed (40 dof) coherence between dp/dt and T from c., with dashed line indicating the 95% significance level. (e) Corresponding phase difference.

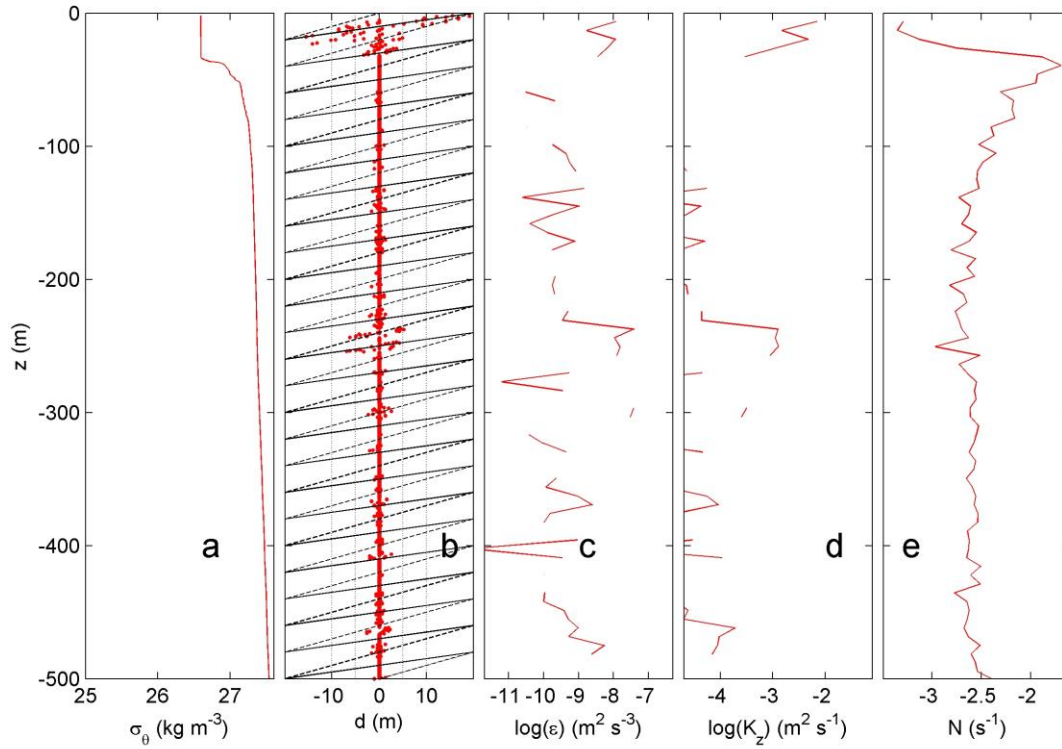


Figure 3. Upper 500 m of turbulence characteristics computed from downcast density anomaly data applying a threshold of $7 \times 10^{-5} \text{ kg m}^{-3}$. Northern station 29, cast 2. (a) Unordered, ‘raw’ profile of density anomaly referenced to the surface. (b) Overturn displacements following reordering of the profiles in a. Slopes $\frac{1}{2}$ (solid lines) and 1 (dashed lines) are indicated. (c) Logarithm of dissipation rate computed from the profiles in a., averaged over 7 m intervals. (d) As c., but for eddy diffusivity. (e) Logarithm of buoyancy frequency computed after reordering the profiles of a.

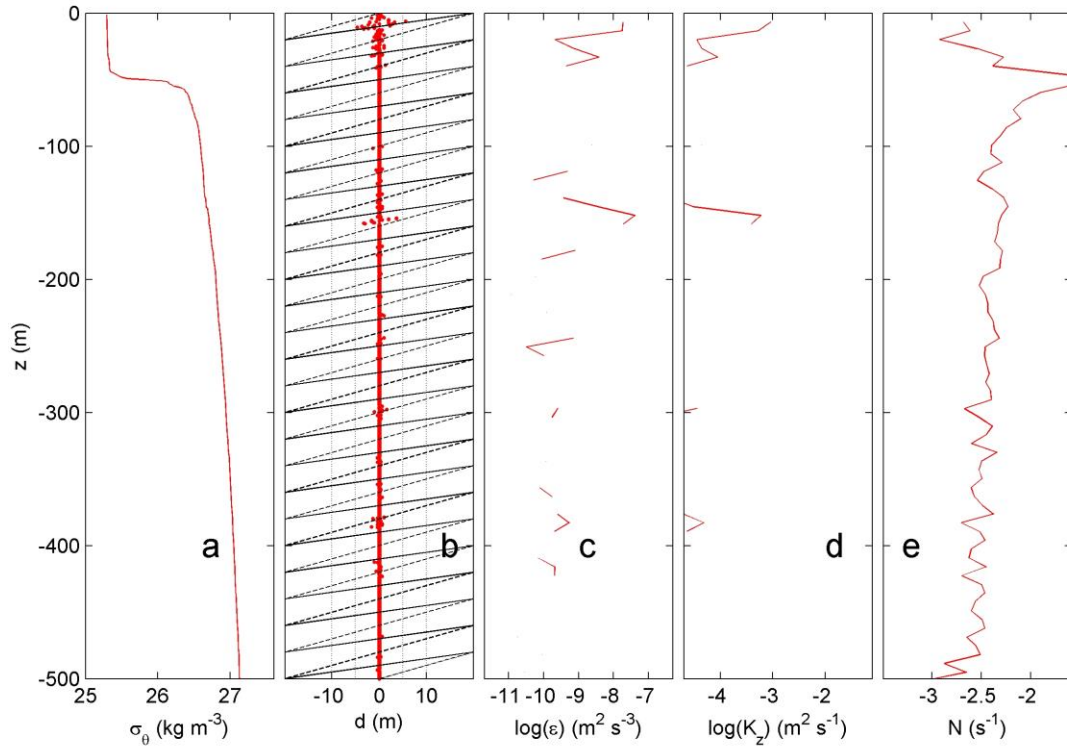


Figure 4. As Fig. 3, but for a southern station. Upper 500 m of turbulence characteristics computed from downcast density anomaly data applying a threshold of $7 \times 10^{-5} \text{ kg m}^{-3}$. Southern station 3, cast 4. (a) Unordered, ‘raw’ profile of density anomaly referenced to the surface. (b) Overturn displacements following reordering of the profiles in a. Slopes $\frac{1}{2}$ (solid lines) and 1 (dashed lines) are indicated. (c) Logarithm of dissipation rate computed from the profiles in a., averaged over 7 m intervals. (d) As c., but for eddy diffusivity. (e) Logarithm of buoyancy frequency computed after reordering the profiles of a.

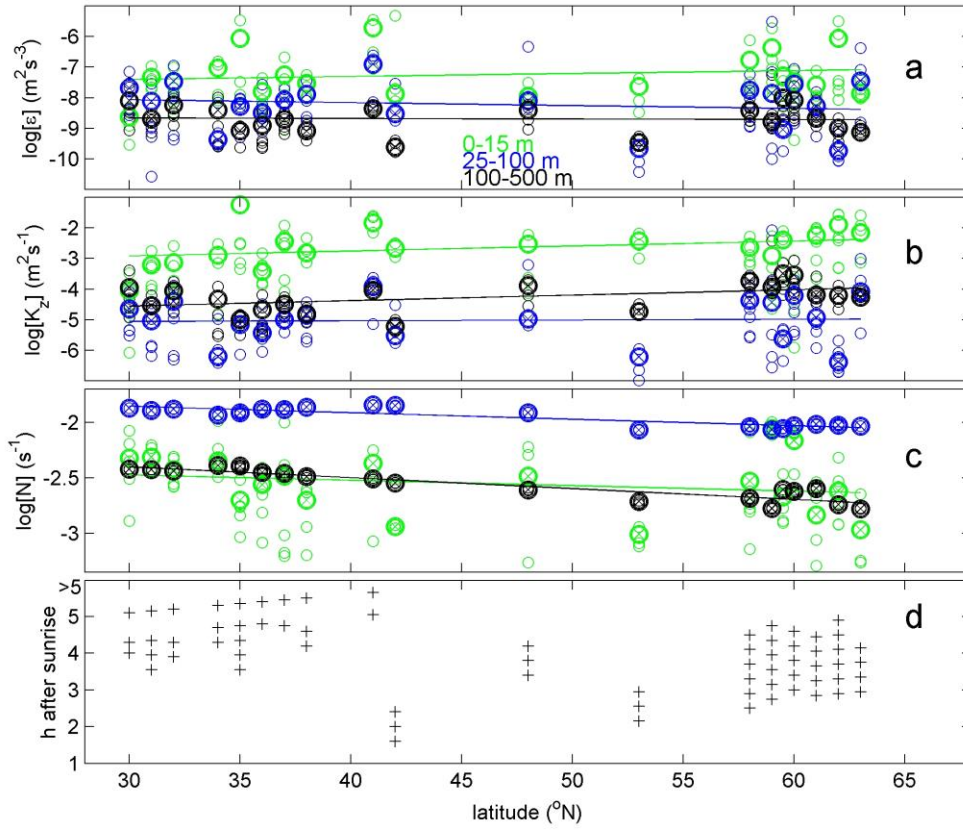


Figure 5. Summer 2017 latitudinal transect along $17 \pm 5^\circ \text{W}$ of turbulence values for upper 15 m averages (green) and averages between $-100 < z < -25$ m (blue, seasonal pycnocline) and $-500 < z < -100$ m (black, more permanent pycnocline) from short yoyos of 3 to 6 CTD-casts. Values are given per cast (o) and station average (heavy circle with x; the size corresponds with \pm the standard error for turbulence parameters). (a) Logarithm of dissipation rate. (b) Logarithm of diffusivity. (c) Logarithm of buoyancy frequency (the small symbols have the size of \pm the standard error). (d) Hour of sampling after sunrise.

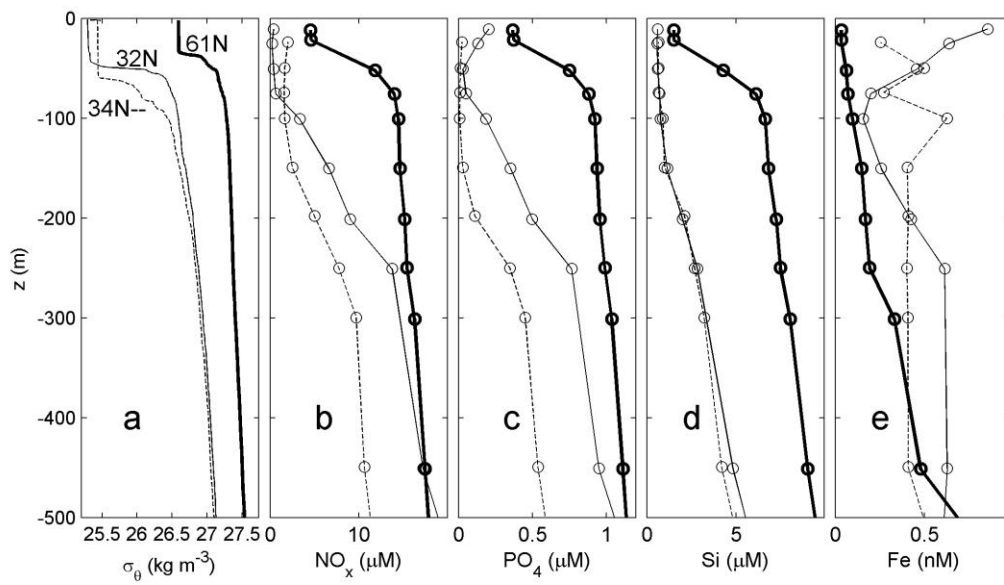


Figure 6. Upper 500 m profiles for stations at three latitudes. (a) Density anomaly referenced to the surface, including profiles from Fig. 3a and 4a. (b) Nitrate plus nitrite. (c) Phosphate. (d) Silicate. (e) Dissolved iron.

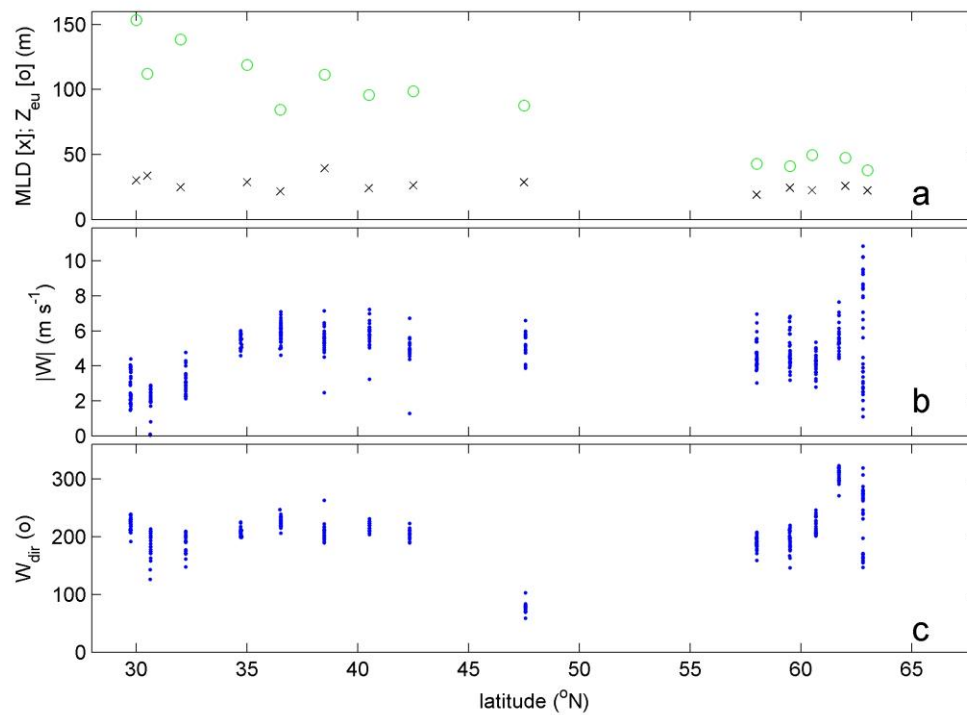


Figure 7. Latitudinal transect of near-surface layers and wind conditions measured at stations during the observational survey. (a) Mixed layer depth (x) and euphotic zone (o). (b) Wind speed. (c) Wind direction.

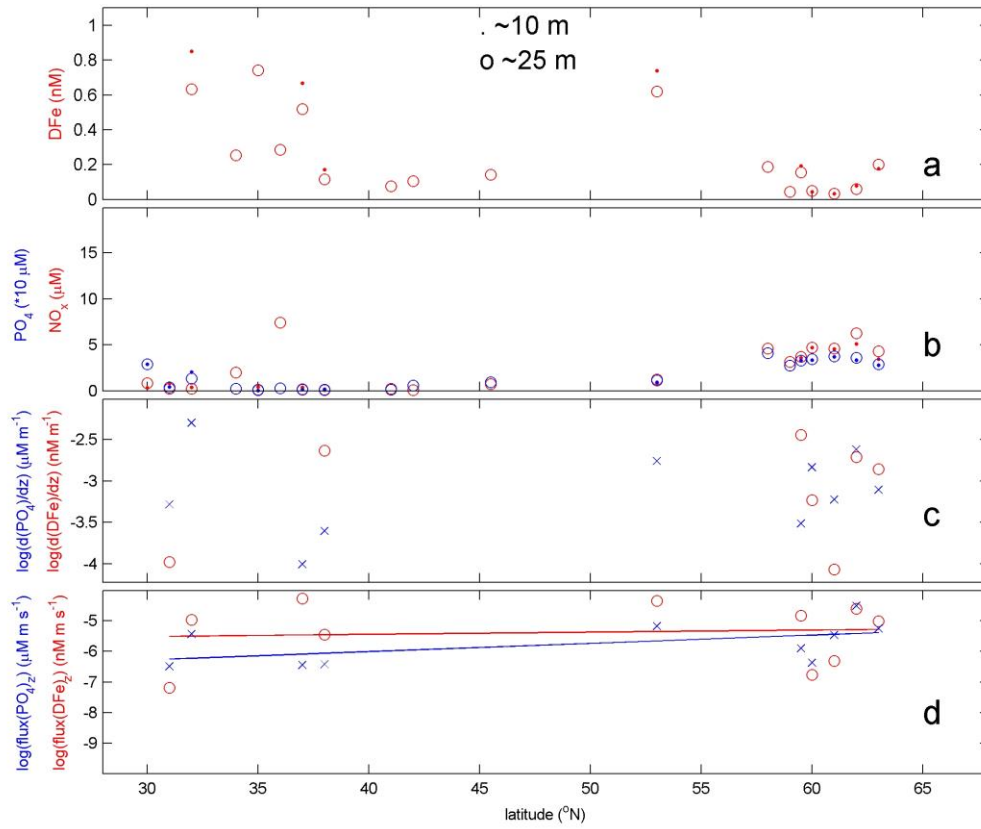


Figure 8. Latitudinal transect of near-surface nutrient concentrations. (a) Dissolved iron. (b) Nitrate plus nitrite (red) and phosphate (blue, scale times 10). (c) Logarithm of vertical gradients of values dissolved iron in a. and phosphate in b. (d). Vertical turbulent fluxes of concentrations in c. using average surface K_z from Fig. 5c.

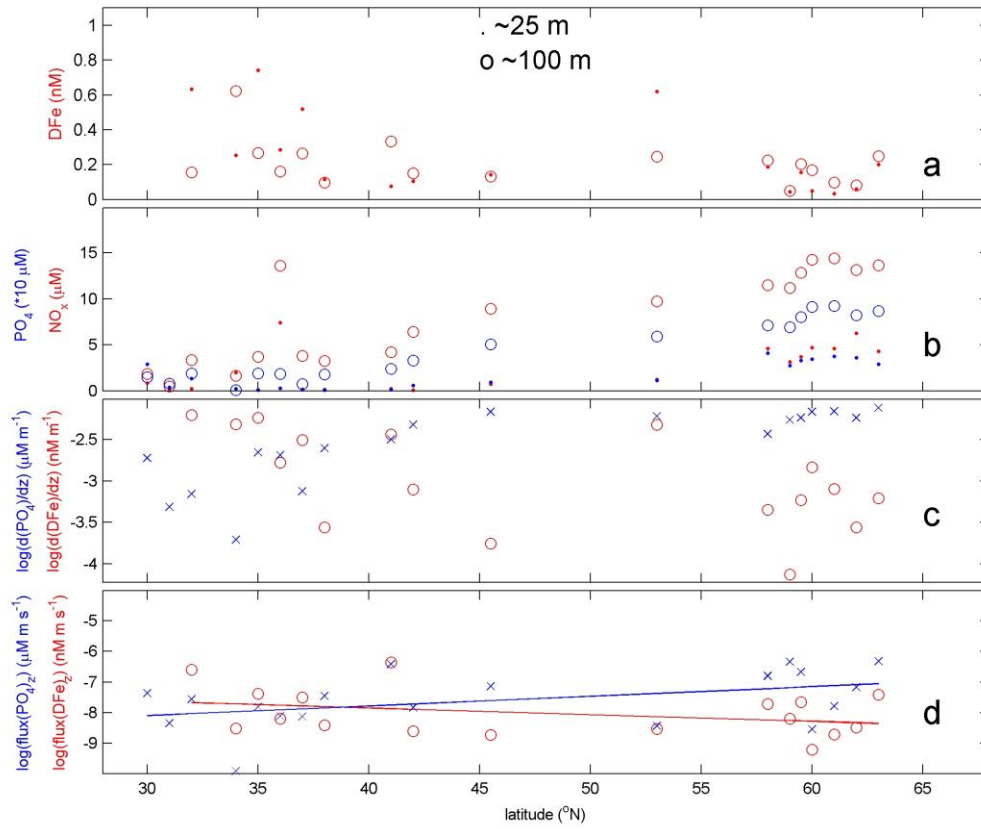


Figure 9. As Fig. 8, but for $-100 < z < -25$ m.

730

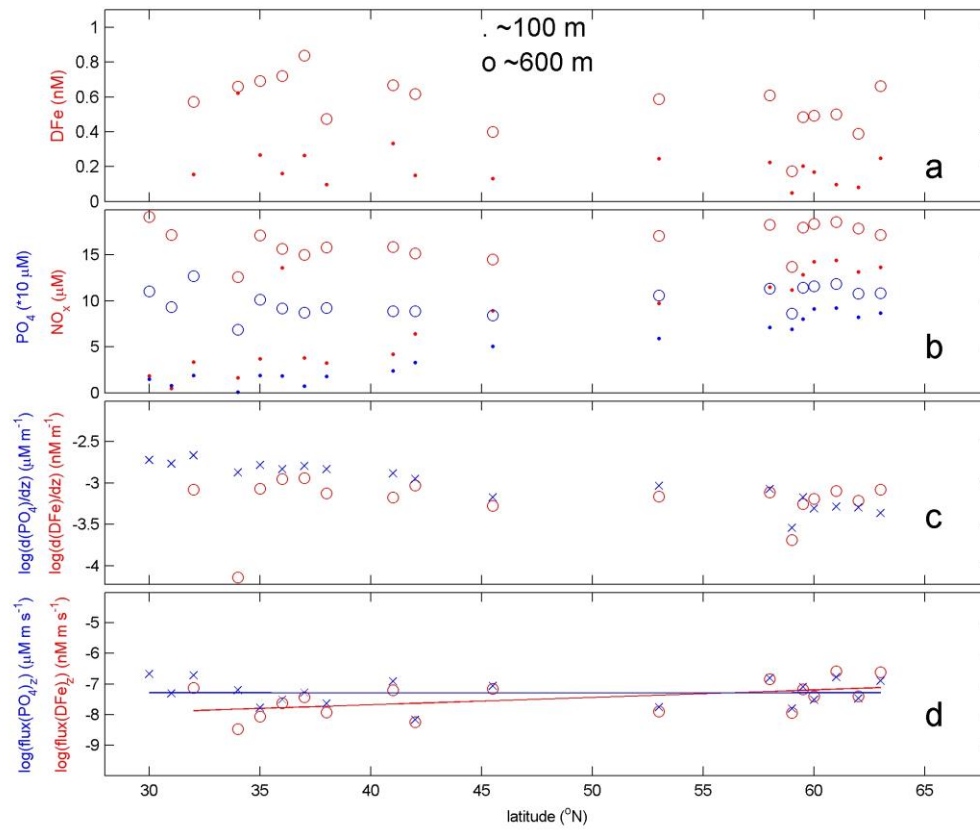


Figure 10. As Fig. 8, but for -600 (few nutrients sampled at 500) $< z < -100$ m.

731
732
733

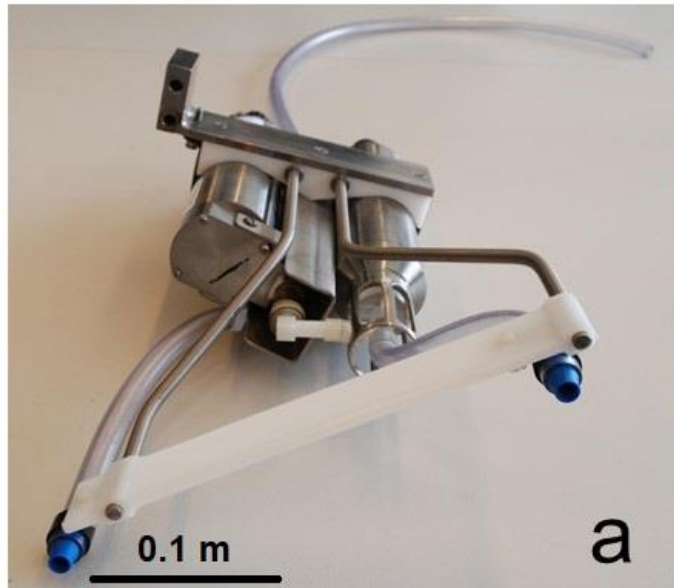


Fig. A1. SBE911 CTD-pump in- and outlet modification following the findings in van Haren and Laan (2016). (a) The T- and C-sensors clamped together with a structure holding in- and outlet pump-tubing of exactly the same diameter, separated at 0.3 m distance in the horizontal plane. (b) The modification of a. mounted in the CTD-frame.

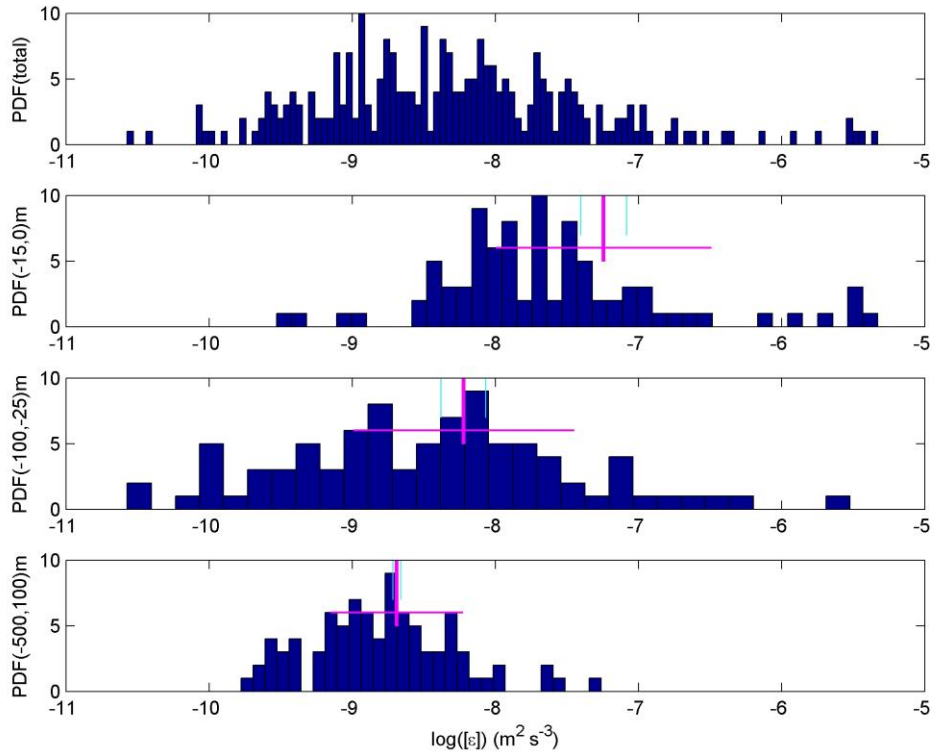


Fig. A2. Probability Density Functions of logarithm of vertically averaged dissipation rate in comparison with latitudinal trend extreme values. (a) Distribution as a function of latitude for all data. (b) As a, but for the upper 15 m averages only. The mean value is given by the vertical purple line, with the horizontal line indicating ± 1 standard deviation. The vertical light-blue lines indicate the best-fit value of the trend for 30° and 63°N . (c) As b, but for averages between $-100 < z < -25$ m. (d) As c, but for averages between $-500 < z < -100$ m.